Pui-Wai Ma, D. R. Mason, S. L. Dudarev

Multiscale Analysis of Dislocation Loops and Voids in Tungsten

Multiscale Analysis of Dislocation Loops and Voids in Tungsten

Pui-Wai Ma, D. R. Mason, S. L. Dudarev

Multiscale Analysis of Dislocation Loops and Voids in Tungsten

Pui-Wai Ma,[*] D. R. Mason, and S. L. Dudarev

UK Atomic Energy Authority, Culham Science Centre, Oxfordshire, OX14 3DB, United Kingdom

We performed *ab initio* density functional theory simulations of $\frac{1}{2}\langle 111 \rangle$ interstitial dislocation loops, closed and open vacancy loops, $\langle 100 \rangle$ interstitial loops and voids in tungsten, using simulation cells involving from 2000 to 2700 atoms. The size of the loops transcends the microscopic scale and reaches the mesoscopic scale where asymptotic elasticity treatment applies. Comparing the formation energies of dislocation vacancy loops and voids, we conclude that a void remains the most energetically favorable vacancy defect over the entire range of sizes investigated here. A closed $\frac{1}{2}\langle 111 \rangle$ vacancy loop is more stable than an open loop if the number of vacancies in the loop is greater than $\sim$45, corresponding to the diameter of the loop of approximately 1.8 nm. We have also computed elastic dipole tensors and relaxation volumes of loops and voids, representing the source terms in continuum models for radiation induced stresses and strains in the material. A detailed analysis of metastable configurations of closed and open vacancy loops performed using molecular statics simulations shows that vacancy loop configurations are not unique, and significant fluctuations of defect structures may occur in the course of microstructural evolution under irradiation.

I. INTRODUCTION

Tungsten is an armour material in the design of the demonstration fusion power plant (DEMO) [1, 2], and it has been chosen as the plasma facing material in the divertor of ITER [3]. It has the highest melting point of all pure metals, high thermal conductivity and low physical sputtering yield, which are important considerations for a material that is expected to be exposed to high heat flux and intense bombardment by light ions from the plasma. Unstable isotopes of tungsten have relatively short half-life [4], enabling the recycling of tungsten exposed to neutron irradiation.

Exposure to neutron irradiation also produces structural defects in the form of Frenkel pairs of vacancies and self-interstitial atoms as well as clusters of defects. These clusters form in high-energy collision cascades, and initially adopt highly non-equilibrium structural configurations that then rapidly relax into the relatively low-energy defect structures like dislocation loops and voids [5–11]. The accumulation of defects gives rise to the degradation of thermal [12] and mechanical [13] properties of tungsten, which in turn limits the lifetime of tungsten components.

Lattice defects also form in ion irradiation experiments that mimic effects of exposure to neutrons [10, 14–18]. *In-situ* transmission electron microscopy (TEM) experiments show that defects formed in thin tungsten foils at low exposure ($\leq$0.01 dpa) over a broad range of temperatures from 30K to 1073K are predominantly $\frac{1}{2}\langle 111 \rangle$ vacancy and interstitial dislocation loops [10, 14]. At higher radiation exposure from 0.4 to 30 dpa, in the broad temperature range from 300K to 1073K, $\frac{1}{2}\langle 111 \rangle$ interstitial loops become more prevalent [15, 16]. Some of the dislocation loops are observed to have a $\langle 100 \rangle$ Burgers vector, but the proportion of these loops diminishes at high temperatures. TEM examination of neutron irradiated tungsten shows the formation of fairly large voids in the material exposed to high dose at elevated temperatures [19].

Although TEM is a powerful tool for observing the formation and evolution of defects under irradiation, its resolution is limited. Dislocation loops that are smaller than 1nm in diameter are difficult to resolve in conventional TEM images. It is also very difficult to identify the nature, vacancy or self-interstitial, of the loops that are smaller than 4nm in diameter. Yet simulations of collision cascades [5–8] suggest that the statistics of sizes of defects follow a power law, which suggests that the majority of defects are below the threshold of resolution of conventional TEM [10, 20].

Long-range elastic interactions between radiation defects [21], and the macroscopic stress fields that populations of defects produce in the materials [22], affect the dynamics of defects and hence the evolution of microstructure [14, 23]. The observed spatially self-organized configurations of dislocation loops [16, 24] can be explored using Langevin defect dynamics and stochastic dislocation dynamics models [24, 25] that treat both the fluctuating thermal motion of defects and dislocations as well as elastic forces acting between the defects. A defect has a self-interaction with a surface due to image forces, leading to a high surface sink strength for mobile defects [26, 27]. However, at a depth below the surface large compared to the size of the loop, elastic interactions between defects can reduce macroscopic diffusivity and prevent escape to the surface [14].

The energy of elastic interaction between localized defects can be evaluated using the elastic dipole tensor and Greens function formalism [21, 28–34], where the elastic dipole tensor fully defines the elastic field of a localized defect in the asymptotic limit [35]. Elements of elastic dipole tensor can now be readily derived from *ab initio* density function theory (DFT) calculations or molecular statics [21, 28–34].

In this study, we perform large scale DFT calcula-

---
[*] leo.ma@ukaea.uk

tions of formation energies, dipole tensors and relaxation volumes of $\frac{1}{2}\langle 111 \rangle$ dislocation loops, including self-interstitial atom (SIA), and vacancy loops in tungsten. We have also investigated $\langle 100 \rangle$ SIA loops, and vacancy clusters and voids. We also consider planar vacancy defects, sometimes called 'open vacancy loops' in the literature [36] - a hypothetical class of defects comprising a disc of vacancies, which if the surfaces were pressed together would form a vacancy dislocation loop. If the elastic and core energy combined for a vacancy loop is greater than the surface energy of the equivalent-sized planar vacancy defect, then there is a thermodynamic driving force from the loop to the planar defect. The transformation may be facilitated in a densely defected environment by fluctuating nanoscale stresses [37] or impinging mobile defects [38].

The sizes of defects explored by DFT transcend the microscopic scale and reach the mesoscopic scale. The computed values do not rely on the fitted semi-empirical interatomic potentials [36] and do not require extrapolating the DFT data [11] from the microscopic limit.

We compare the DFT data with molecular statics calculations performed using interatomic potential as well as with analytical expressions derived from linear elasticity. Further molecular statics analysis is performed to explore the metastable states involving the transition between closed and open vacancy loops. The results show that while the asymptotic linear elasticity treatment retains its accuracy on the mesoscopic scale and approximates the energy of loops and void well, the energy of both types of defects contains a substantial non-elastic contribution associated with dislocation cores or open surfaces. This also shows that the DFT data, describing dislocation loops and voids on the mesoscale, are readily transferable to the continuum scale simulations.

II. *AB INITIO* CALCULATIONS

Density functional theory calculations described in this study were performed using the OpenMX *ab initio* simulations package [39–42]. OpenMX is a DFT simulation program using norm-conserving pseudopotentials [43–47] and pseudo-atomic localized basis functions [39, 40]. It is primarily designed for large-scale DFT calculations on parallel computers using MPI or MPI/OpenMP hybrid parallelism. To accelerate the large-scale simulations we have inoculated the Eigenvalue SoLvers for Petaflop-Applications (ELPA) [48, 49] version 2018.05.001 to OpenMX. ELPA provides highly scalable and efficient means for finding eigenvalues and eigenstates. The MPI/OpenMP hybrid implementation of ELPA also substantially reduces the memory requirements, enabling modelling metallic systems containing thousands of atoms.

The pseudopotential includes the $5p$, $5d$, and $6s$ states of a tungsten atom as valence states, involving in total 12 valence electrons. A set of basis functions corresponding to two s, two p and two d optimized atomic orbitals is used in the calculations, with the cutoff radius of 7 Bohr radii a_B. The exchange correlation functional is taken in the generalized gradient approximation (GGA), according to Perdew, Burke and Ernzerhof (PBE) [50, 51]. Charge density is represented on regular real-space grid, where the distance between the grid point is always smaller than 0.1 Å. The maximum force acting on an atom in a relaxed ionic configuration is assumed to be less that 1×10^{-4} Hartree/Bohr radius. Since the simulation boxes considered in this study are all very large, in k-space the calculations only involve one gamma point.

We created perfect BCC cubic cells containing 2000 and 2662 atoms, and relaxed them to the stress free condition. Then, we fixed the size of the simulation cell, and created a defect inside it by adding or removing atoms. In this way, we created $\frac{1}{2}\langle 111 \rangle$ SIA, vacancy open and vacancy closed loops, $\langle 100 \rangle$ SIA loops and voids. We only considered pure prismatic loops, where the normal vector to the habit plane of a loop is collinear with the Burgers vector.

When treating $\mathbf{b} = \frac{a}{2}\langle 111 \rangle$ prismatic loops, we created hexagonal loops with 7 and 19 atoms in the 2000 atoms cells, and loops with 37 and 61 atoms in the 2662 atoms cells. SIA loops were created by inserting an extra atom in each neighbouring atomic string running in the [111] direction. Open loops were created by simply removing atoms from the simulation cells. Closed loops were created by removing atoms, followed by pulling atoms in the centre of the loop close together. The two upper and two lower layers of atoms, corresponding to the removed layer of atoms and within the loop radius, were moved in the Burgers vector direction such that the spacing between all layers between the third upper and lower layers were equally spaced. When considering $\langle 100 \rangle$ SIA loops, we created square loops with 13 and 25 atoms in 2000 atom cells, and loops with 41 and 61 atoms in 2662 atoms cells. Voids with 9, 27, 51, 59, 65 and 89 atoms were all created in 2000 atoms cells.

Before performing ionic relaxation using OpenMX, we relaxed all the configuration using the conjugate gradient minimisation algorithm implemented in LAMMPS [52]. We used the Mason-Nguyen-Manh-Becquart (MNB) interatomic potential for tungsten [53], which produces energetically stable closed vacancy loop structures even when the loop is relatively small.

The formation energy of a defect can be written as [31–34]:

$$E_D^F = [E_D(N_D) - E^{app}] - \frac{N_D}{N_{perf}} E_{perf}(N_{perf}) - E_{el}^{corr}, \tag{1}$$

where N_{perf} is the number of atoms in a perfect lattice cell, N_D is the number of atoms in a simulation box containing a defect. E_D is the total energy of the cell containing a defect, E^{app} is the energy associated with applied strain, E_{perf} is the energy of the perfect lattice cell, and E_{el}^{corr} is a correction term resulting from the condition of vanishing global average strain and pe-

	C_{11} (GPa)	C_{12} (GPa)	C_{44} (GPa)	a (Å)
OpenMX	535.23	191.09	150.37	3.199
VASP [31]	518.26	199.77	142.09	3.184
VASP [54]	517.4	199.3	142.3	3.186
MNB [53]	521.85	204.11	160.62	3.165
GAP [55]	526	200	149	3.1852
Exp. [56]	522.24	204.4	160.6	3.16

TABLE I. Elastic constants and the bcc lattice parameter of tungsten calculated using OpenMX, VASP [31, 54], the MNB many-body potential [53], the Gaussian Approximation Potential (GAP) [55]. The computed values are compared with the corresponding experimental values taken from Ref. [56].

riodic boundary conditions. $E^{app} = 0$ here, because we keep the boundaries of the simulation cells fixed, and do not relax the boundaries of the cells containing defects. E_{el}^{corr} can be evaluated numerically if the elastic dipole tensor P_{ij} and and elastic constant tensor C_{ijkl} are known [21, 28, 29, 31–34]. E_{el}^{corr} was evaluated using the CALANIE code described elsewhere [34].

The elastic dipole tensor of a defect can be evaluated from the macrostress $\bar{\sigma}_{ij}$ developing in the simulation cell as a result of formation of a defect in it [21, 28, 29, 31–34], namely

$$P_{ij} = - \int_{V_{cell}} \sigma_{ij}(\mathbf{r}) dV = -V_{cell} \bar{\sigma}_{ij}, \qquad (2)$$

where σ_{ij} is the spatially varying stress in a periodically translated simulation cell, and $\bar{\sigma}_{ij}$ is the average stress in the cell. The above formula assumes the validity of the linear elasticity approximation. It also assumes that atomic displacements at the cell boundary are well approximated by linear elasticity.

The relaxation volume of a defect equals the volume change of the elastic material resulting from the elastic relaxation of the position of atoms around the defect [35]. The volume change is measured with respect to the perfect crystal reference state. For example, the relaxation volume of a vacancy is negative because the material surrounding the vacancy relaxes towards it. The relaxation volume tensor of a defect can be related to its dipole tensor as [21, 35]

$$\Omega_{ij} = S_{ijkl} P_{kl}, \qquad (3)$$

where $\mathbf{S} = \mathbf{C}^{-1}$ is the elastic compliance tensor, satisfying the condition $C_{ijkl} S_{klmn} = \frac{1}{2}(\delta_{im}\delta_{jn} + \delta_{in}\delta_{jm})$. The relaxation volume of the defect can be computed by taking the trace of tensor Ω_{ij}, namely [35]

$$\Omega_{rel} = \text{Tr}(\Omega_{ij}) = \Omega_{11} + \Omega_{22} + \Omega_{33}. \qquad (4)$$

The elements of the elastic constant tensor, C_{ijkl}, can be computed using the Le Page and Saxe method [57].
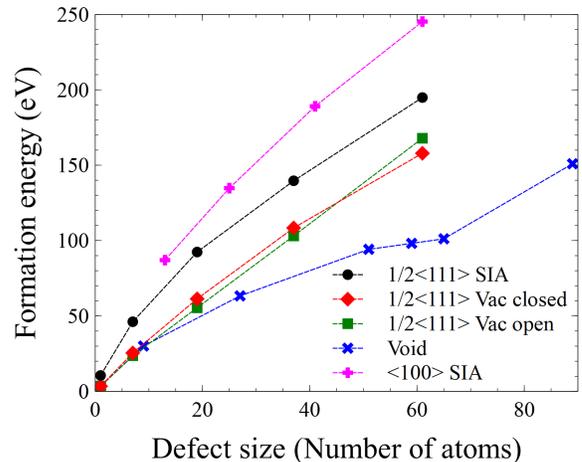
FIG. 1. Formation energies of $\frac{1}{2}\langle 111 \rangle$ SIA, vacancy open and vacancy closed loops, $\langle 100 \rangle$ SIA loops and voids, calculated using density functional theory package OpenMX. Lines connecting the data points are not interpolations, rather they are shown to guide the eye.

We performed the calculations using a 2-atom simulation cell and $21 \times 21 \times 21$ k-point mesh. In the Voigt notation, we find $C_{11} = 535.23$ GPa, $C_{12} = 191.09$ GPa, $C_{44} = 150.37$ GPa, and the equilibrium lattice constant of $a = 3.199$ Å. These values compare well with the experimental values [56] as well as with values derived from earlier VASP calculations [31, 54]. The *ab initio* and experimental values are summarised in table I, together with the values found using the MNB many-body interatomic potential [53].

We also performed several other benchmark tests. We calculated the formation energy of configurations with a vacancy and a self-interstitial atom (SIA) in a $\langle 111 \rangle$ dumbbell configuration using supercells containing $4 \times 4 \times 4$ bcc unit cells and a $5 \times 5 \times 5$ k-point mesh. The formation energy of vacancy found in the simulations is 3.428 eV whereas the formation energy of a $\langle 111 \rangle$ dumbbell is 10.557 eV. These values agree well with the VASP data evaluated using the PAW potential [31], where the formation energy of a vacancy was found to be 3.223 eV, and the formation energy of a $\langle 111 \rangle$ dumbbell 10.287 eV.

III. DFT RESULTS AND COMPARISON WITH LINEAR ELASTICITY

The formation energies and elastic dipole tensors of $\frac{1}{2}\langle 111 \rangle$ self-interstitial atom (SIA) dislocation loops, open and closed vacancy loops, $\langle 100 \rangle$ SIA loops and voids, calculated using OpenMX, are shown in Figs. 1 and 2. A spherical void, according to the data, remains the most stable vacancy cluster configuration. The $\langle 100 \rangle$ SIA loops have higher formation energies than $\frac{1}{2}\langle 111 \rangle$ SIA loops.

One of the key findings of this study is the explicit demonstration of that the relative stability of $\frac{1}{2}\langle 111 \rangle$
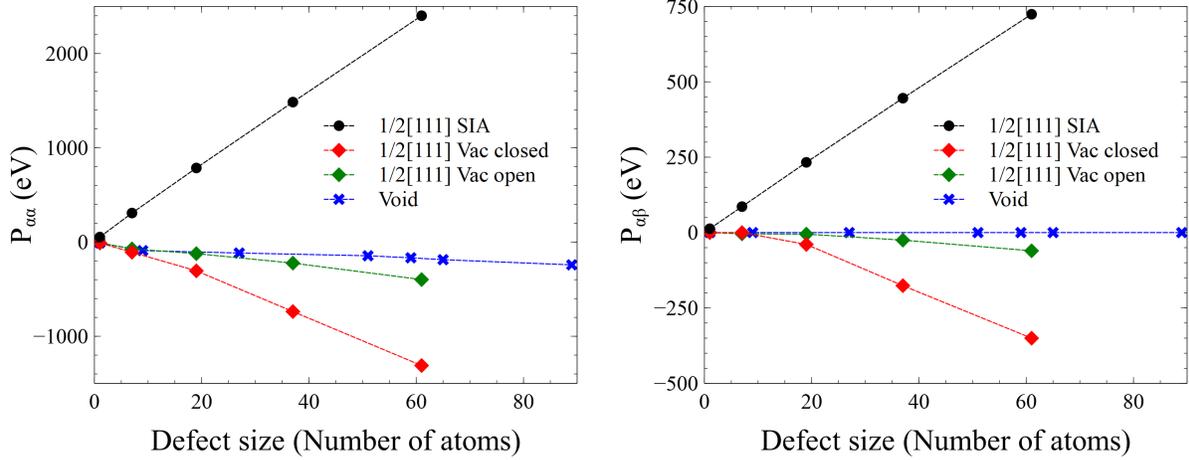
FIG. 2. Elastic dipole tensors of $\frac{1}{2}\langle 111 \rangle$ SIA, open and vacancy closed vacancy loops, and voids, computed using OpenMX. The Burgers vector of loops $\mathbf{b} = \frac{1}{2}[111]$. $P_{\alpha\alpha}$ are the diagonal elements of the elastic dipole tensor, whereas $P_{\alpha\beta}$ are the off-diagonal elements.
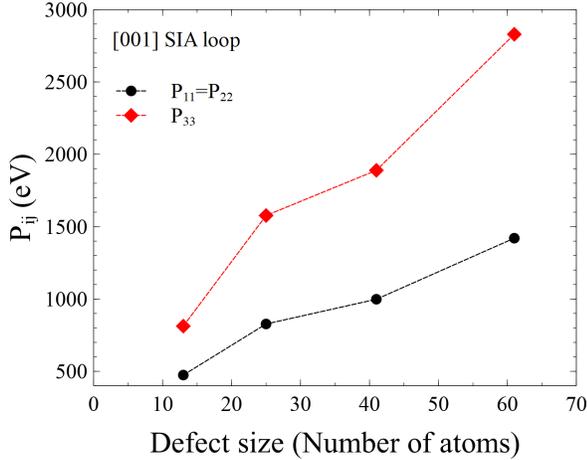
FIG. 3. Elastic dipole tensors of $\langle 100 \rangle$ SIA loops with the Burgers vector $\mathbf{b} = [001]$, calculated using OpenMX. All the elements not shown in the Figure, vanish because of symmetry considerations.

closed and open vacancy loops changes when the loops contain approximately 45 vacancies. The formation energy of a 37 vacancy planar defect is lower than that the corresponding closed loop, whereas the formation energy of a 61 vacancy closed loop is lower than that of the corresponding planar defect. The atomic configurations of 37- and 61- vacancy loops are show in Fig. 4. They were generated using AtomEye [58] by filtering out the nearly perfect lattice atoms using a central symmetry criterion.

We can compare the DFT values with analytical expressions for the energy of defects derived from the theory of linear elasticity [59]. The purpose of such a comparison is not only to establish the range of validity of elasticity theory, but also to produce explicit analytical

expressions valid in the asymptotic limit where the size of dislocation loops is large.

The formation energy of an SIA or a closed vacancy dislocation loop in the asymptotic continuum limit, described by the elasticity approximation, can be written as a sum of contributions from the dislocation segments forming the perimeter of the loop [59] or, in a generalised form, as a contour integral over the perimeter of the loop as [60]

$$E = \left[\oint E(\mathbf{t}) d\mathbf{t} \right] \ln \left(\frac{\tilde{R}}{\delta} \right) + \oint E_\delta(\mathbf{t}) d\mathbf{t} + \oint E_c(\mathbf{t}) d\mathbf{t}, \quad (5)$$

where $\tilde{R}$ is a measure of loop linear size, for example the loop radius, and δ is the effective radius of the dislocation core where the elasticity approximation fails. $E(\mathbf{t})$ is the pre-logarithmic factor, defining the magnitude of elastic self-energy per unit length of the dislocation line with Burgers vector $\mathbf{b}$ and tangent vector $\mathbf{t}$. This pre-logarithmic factor can be computed from the tensor of elastic constants C_{ijkl} of the material using the equation [59, 60]

$$E(\mathbf{t}) = \frac{1}{2\pi} b_i b_m n_j n_q C_{ijkl} C_{npmq}$$
$$\times \operatorname{Im} \left[\sum_{\alpha=1}^{3} \kappa_p^{(\alpha)} \kappa_l^{(\alpha)} \frac{N_{kn}(\boldsymbol{\kappa}^{(\alpha)})}{n_s \frac{\partial D(\boldsymbol{\kappa}^{(\alpha)})}{\partial \kappa_s}} \right]. \quad (6)$$

Here $D(\boldsymbol{\kappa})$ is the determinant of matrix $L_{ik}(\boldsymbol{\kappa}) = C_{ijkl}\kappa_j\kappa_l$, and index α refers to the three roots of the sixth-order algebraic equation $D(\boldsymbol{\kappa}) = 0$, which are situated in the upper half of the complex plane. In equation (5), $E_\delta(\mathbf{t})$ and $E_c(\mathbf{t})$ are the core-traction and non-linear core energy per dislocation unit length, respectively. Although in principle the core traction term $E_\delta(\mathbf{t})$ can also be evaluated explicitly from elasticity [59], and $E_c(\mathbf{t})$ can
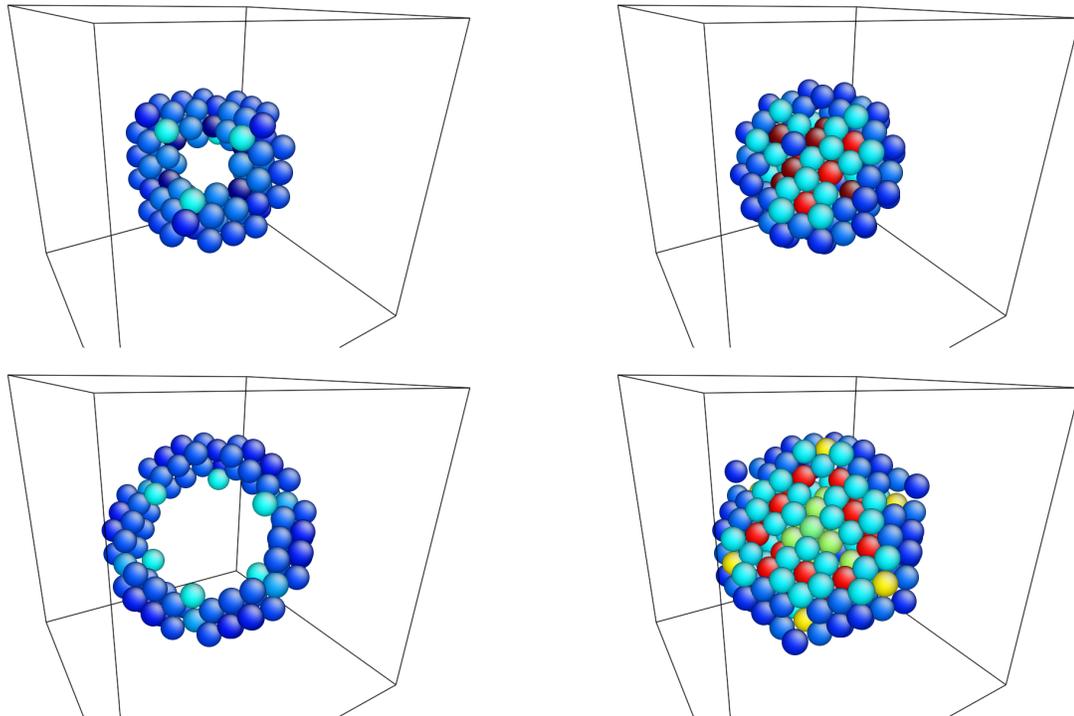
FIG. 4. Atomic configuration of a circular vacancy $\frac{1}{2}\langle 111 \rangle$ loop. Bulk atoms were filtered out according to the central symmetry parameter criterion. (Top left) 37 atoms closed loop. (Top right) 37 atoms open loop. (Bottom left) 61 atoms closed loop. (Bottom right) 61 atoms open loop.

be determined by comparing the elastic energy with the energy derived from discrete atomistic simulations, in practice only the first term $E(\mathbf{t})$ in equation (5) should be treated as a meaningful and reasonably well defined quantity.

In the isotropic elasticity limit $E(\mathbf{t})$ does not depend on the direction of the tangent vector of the dislocation line, and for an edge dislocation this factor equals [61]

$$E(\mathbf{t}) = \frac{\mu \mathbf{b}^2}{4\pi(1-\nu)}, \qquad (7)$$

where μ is the shear modulus and ν is the Poisson ratio of the material.

To assess how strongly the energy of edge dislocations, forming the perimeter of a pure prismatic dislocation loop, depends on the orientation of the dislocation line with respect to the crystal lattice, in Figure 5 we show how the pre-logarithmic factor $E(\mathbf{t})$ varies as the dislocation line rotates around its Burgers vector. In the nearly exactly isotropic elasticity limit, corresponding to the values of elastic constants observed experimentally at ambient conditions, the energy of either $\frac{1}{2}\langle 111 \rangle$ or $\langle 001 \rangle$ edge dislocations barely depends on the orientation of the tangent vector of the dislocation line. Although the empirical potential or DFT models predict tungsten as being elastically anisotropic, Figure 5 shows that the degree of elastic anisotropy remains fairly small in all the cases considered in this study. This justifies the use of

	E_{111}	E_{001}	$\frac{E_{001}}{E_{111}}$	$\mathcal{E}_{111}$	$\mathcal{E}_{001}$
OpenMX	0.833	1.130	1.356	3.769	5.110
VASP [31]	0.788	1.065	1.352	3.548	4.797
VASP [54]	0.788	1.065	1.352	3.550	4.800
MNB [53]	0.829	1.104	1.332	3.711	4.943
GAP [55]	0.813	1.097	1.348	3.662	4.937
Exp.	0.827	1.101	1.332	3.696	4.923

TABLE II. Values of pre-logarithmic factors in the expression for the orientation-average line energy of $\frac{1}{2}\langle 111 \rangle$ and $\langle 001 \rangle$ edge dislocations computed using anisotropic elasticity [59, 60], and given in eV/Å units. The last two columns show values of parameter $\mathcal{E}$ (in eV) in the leading term of the asymptotic elasticity expression for the energy of a dislocation loop as a function of the number N of point defects that the loop contains $E(N) \sim \mathcal{E}\sqrt{N}\ln(N)$, see text for more detail. Note that in the isotropic elasticity approximation, where $C_{11} - C_{12} = 2C_{44}$, the ratio of elastic energies of line $\langle 001 \rangle$ and $\frac{1}{2}\langle 111 \rangle$ edge dislocations equals 4/3=1.3333.. [60], and the fact that the values given in the third column are very close to 4/3 shows that all the models explored in this study predict tungsten as being nearly elastically isotropic.

orientation-average values of $E(\mathbf{t})$, which we use below when referring to the energy of either $\frac{1}{2}\langle 111 \rangle$ or $\langle 001 \rangle$ edge dislocations.
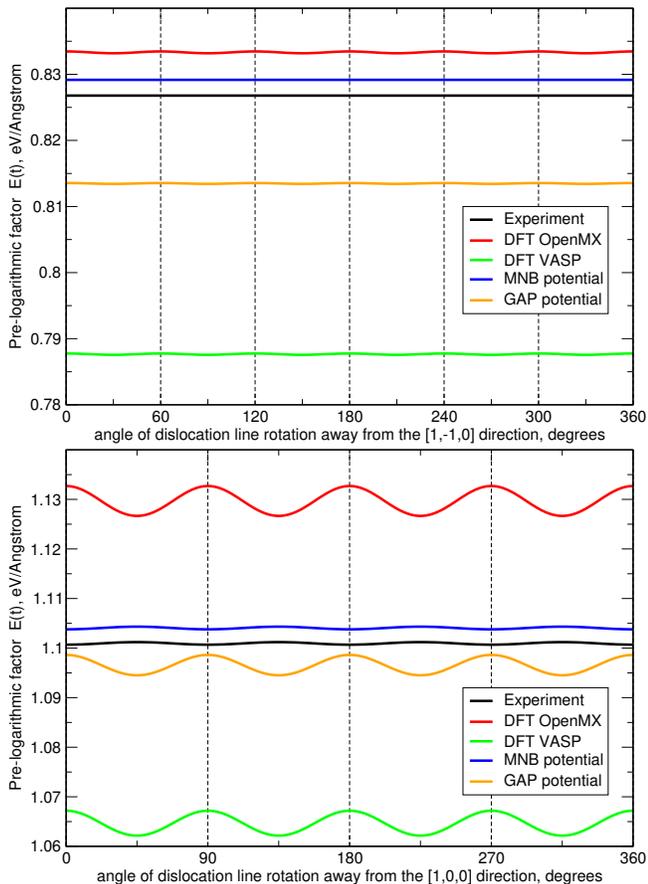
FIG. 5. Pre-logarithmic factor $E(\mathbf{t})$ entering the first term of equation (5) plotted as a function of the orientation of the tangent vector of the dislocation line. The curves are computed using equation (6) for the $\frac{1}{2}\langle 111 \rangle$ and $\langle 001 \rangle$ edge dislocations using the elastic parameters given in Table I. The orientation-average values of pre-logarithmic factors are summarised in Table II.

Through equation (5), we can relate the elastic energy of dislocation lines forming the perimeter of a dislocation loop, to the formation energy of the loop as a whole, assuming that the elastic field of the loop dominates its formation energy. In a bcc lattice with lattice parameter a, the volume per atom equals $\Omega_0 = a^3/2$. Since the magnitude of the Burgers vector of a $\frac{1}{2}\langle 111 \rangle$ loop is $|\mathbf{b}| = a\sqrt{3}/2$, and the magnitude of the Burgers vector of a $\langle 001 \rangle$ loop is $|\mathbf{b}| = a$, we find that the area per atom, viewed in projection along the Burgers vector direction, is $a^2/\sqrt{3}$ for a $\frac{1}{2}\langle 111 \rangle$ loop, and $a^2/2$ for a $\langle 001 \rangle$ loop.

Since the area of a hexagonal dislocation loop with side L is $3\sqrt{3}L^2/2$, we can relate the number of atoms N in a hexagonal loop to its area and length L as $N = 9L^2/2a^2$. From this expression, we find the elastic energy of a hexagonal loop as

$$E_{hex}(N) = 2\sqrt{2}a\sqrt{N}\, E_{disl}(N), \qquad (8)$$

where E_{disl} is the energy per unit length of a dislocation line forming the perimeter of the loop. From equation

(5) this is seen to be $E_{disl} = \ln(\tilde{R}/\delta) \sim (1/2)\ln N$, and hence the energy of a hexagonal $\frac{1}{2}\langle 111 \rangle$ dislocation loop is

$$E_{hex}(N) \sim \sqrt{2}aE_{111}\sqrt{N}\ln(N) + O(\sqrt{N}). \qquad (9)$$

Similarly, for a square $\langle 001 \rangle$ dislocation loop we find that the side L of the loop is related to the number N of atoms that the loop contains as $N = 2L^2/a^2$. Since the length of the perimeter of a square loop is $4L$, we find that the elastic energy of a square $\langle 001 \rangle$ loop can be expressed in terms of the energy of line dislocations forming its perimeter as

$$E_{square}(N) \sim \sqrt{2}aE_{001}\sqrt{N}\ln(N) + O(\sqrt{N}). \qquad (10)$$

This expression is formally identical to the expression for the energy of a hexagonal loop containing the same number of atoms (9) above, and this enables using the same simple asymptotic formula for the elastic energy of dislocation loops of both types $E(N) \sim \mathcal{E}\sqrt{N}\ln(N)$. Values of parameter $\mathcal{E}$ in this formula, derived from the orientation-average line energies shown in Figure 5, are given in Table II.

Curves obtained by fitting Eq. (5) to the data derived from OpenMX and MNB potential calculations are shown in Fig. 6. To improve the quality of the fit in the mesoscopic range of values of N, we also include the core energy term $\sim \sqrt{N}$ and a constant term particularly significant at $N \approx 1$, arriving at

$$E_{loop}(N) = \mathcal{E}\sqrt{N}\ln N + \mathcal{E}_1\sqrt{N} + \mathcal{E}_2. \qquad (11)$$

Parameters $\mathcal{E}_1, \mathcal{E}_2$ were fitted using linear least squares to the form

$$\frac{E_{loop}(N)}{\sqrt{N}} - \mathcal{E}\ln N = \mathcal{E}_1 + \frac{\mathcal{E}_2}{\sqrt{N}}. \qquad (12)$$

The values of parameters derived from fitting and referring to the various simulation models explored in this study, are summarised in table III. A simple examination of values given in the table shows that the leading term in the asymptotic expression becomes dominant for $N \geq 30$, and this condition approximately defines the range of validity of the elasticity approximation.

We should like to point out that the above analysis highlights a general fundamental point associated with the linear elasticity approximation, namely that the total energy values derived from the elasticity theory are valid only in the *asymptotic* sense. For example, the elasticity treatment enables evaluating the leading term in the expression for the energy of a dislocation loop (11). However, the ratio of the leading term to the second term in equation (11) is $(\mathcal{E}/\mathcal{E}_1)\ln N$. This shows that only in the macroscopic limit where N is very large that the elastic part of the energy of the loop (the first term in (11)) becomes much larger than the contribution to the energy from the dislocation core (the second term in (11)).
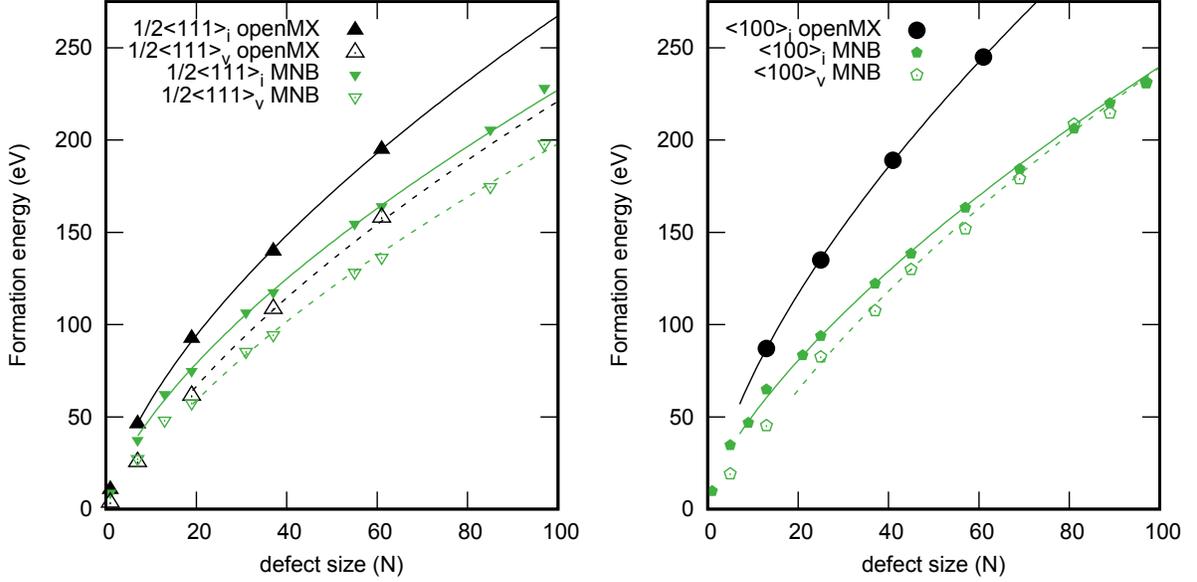
FIG. 6. Formation energies of prismatic SIA and vacancy dislocation loops evaluated using OpenMX and MNB potential, and fitted according to Eq. 5.

Structure	Method	$\mathcal{E}$	$\mathcal{E}_1$	$\mathcal{E}_2$
$\frac{1}{2}\langle 111\rangle[111]_i$	DFT OpenMX	3.769	9.08 ± 0.36	3.0 ± 1.5
$\frac{1}{2}\langle 111\rangle[111]_i$	DFT VASP [54]	3.550	13.33 ± 0.75	-9.2 ± 2.6
$\frac{1}{2}\langle 111\rangle[111]_i$	GAP [55]	3.662	8.93 ± 0.43	3.7 ± 1.5
$\frac{1}{2}\langle 111\rangle[111]_i$	MNB [53]	3.711	4.89 ± 0.09	7.3 ± 0.7
$\frac{1}{2}\langle 111\rangle[111]_v$	DFT OpenMX	3.769	5.70 ± 0.54	-9.5 ± 2.2
$\frac{1}{2}\langle 111\rangle[111]_v$	GAP	3.662	6.68 ± 0.20	-14.6 ± 1.4
$\frac{1}{2}\langle 111\rangle[111]_v$	MNB	3.711	3.26 ± 0.09	-5.5 ± 0.9
$\langle 100\rangle[100]_i$	DFT OpenMX	5.110	9.82 ± 0.16	4.2 ± 0.8
$\langle 100\rangle[100]_i$	DFT VASP	4.800	9.87 ± 0.55	1.2 ± 1.8
$\langle 100\rangle[100]_i$	GAP	4.937	10.25 ± 0.37	0.5 ± 1.3
$\langle 100\rangle[100]_i$	MNB	4.943	-0.38 ± 0.11	16.0 ± 0.9
$\langle 100\rangle[100]_v$	GAP	4.937	5.07 ± 0.17	-29.1 ± 1.3
$\langle 100\rangle[100]_v$	MNB	4.943	2.45 ± 0.19	-12.7 ± 1.8
$\langle 100\rangle[211]_v$	MNB	3.4 ± 0.6	6.1 ± 3.8	-10 ± 10

TABLE III. Empirically determined fits to the formation energy of interstitial (i) and vacancy (v) closed dislocation loops considered in this work. Fits are in the form $E_{loops}(N) = \mathcal{E}\sqrt{N}\ln N + \mathcal{E}_1\sqrt{N} + \mathcal{E}_2$. Note that when habit plane normal and Burgers vector are parallel, $\mathcal{E}$ is fixed by crystal and elastic properties of the material, $\mathcal{E}_1$ is a measure of non-linear core energies, and $\mathcal{E}_2$ is an offset. Fits for interstitial loops were taken for sizes $N \geq 7$. For the MNB potential, fits for vacancy closed loops were taken for sizes $N \geq 19$. The error bars are 68% confidence intervals (one standard deviation).

Neglecting the dislocation core effects, the dipole tensor of a dislocation loop can be written as [21]:

$$P_{ij} = C_{ijkl}b_k A_l, \tag{13}$$

where $\mathbf{b}$ is the Burgers vector and $\mathbf{A}$ is the area vector of a loop. The relaxation volume of a large dislocation loop simply equals its geometric volume, see equation (43) of [62] and the derivation given in [21]

$$\Omega_{rel} = \mathbf{b} \cdot \mathbf{A} = \pm N\Omega_0 = V, \tag{14}$$

where N is the number of point defects that form the dislocation loop, and $\Omega_0 = a^3/2$ is the atomic volume. The relaxation volume is positive for a loop of interstitial type and negative for a loop of vacancy type [21, 62]. It is possible to derive an explicit expression for P_{ij} as a function of N, and similarly to the above expression for the relaxation volume, and in the elasticity approximation it is expected that the dipole tensor of a loop should vary linearly as a function of N.
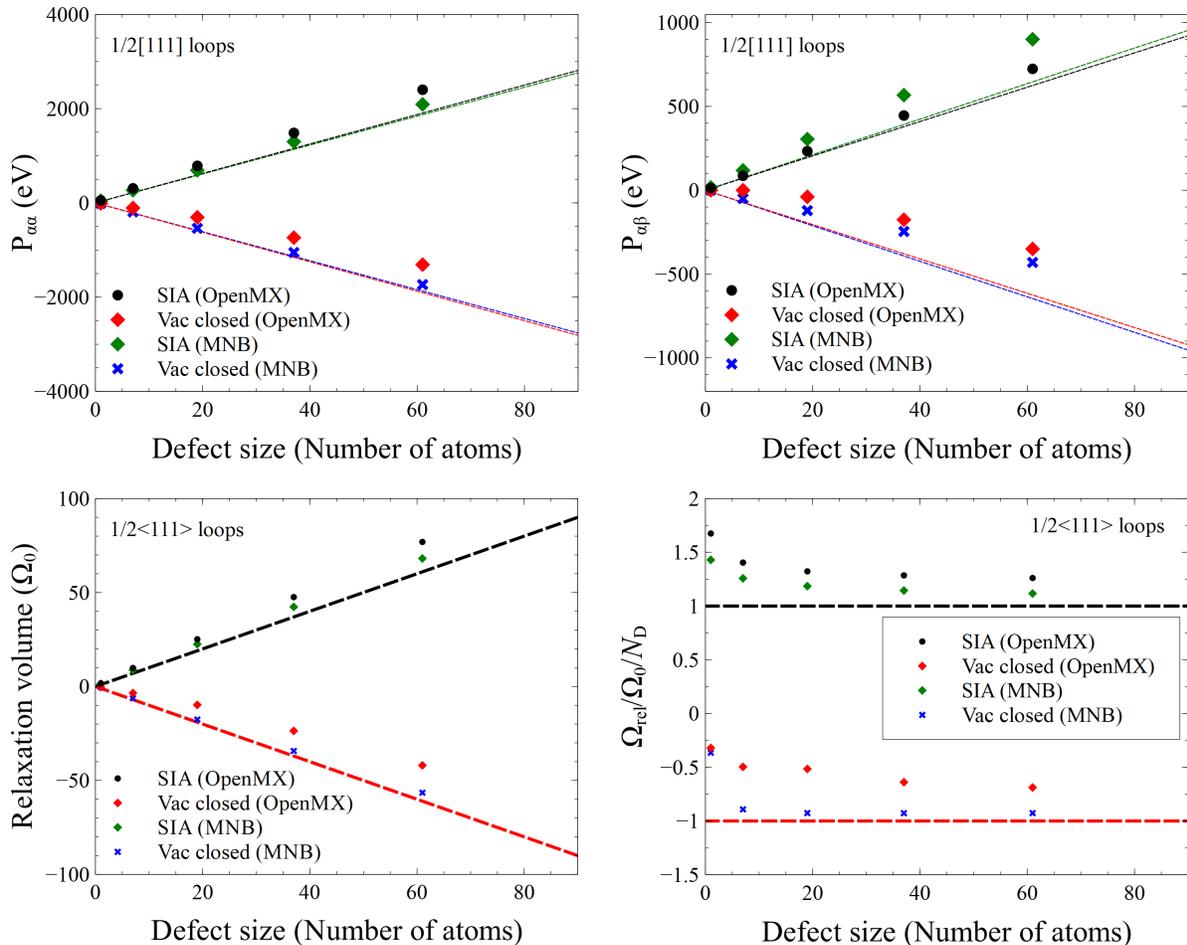
FIG. 7. Calculated elastic dipole tensor P_{ij} and relaxation volume of $\frac{1}{2}\langle 111\rangle$ SIA and vacancy closed loops with $\mathbf{b} = \frac{1}{2}[111]$ using OpenMX and MNB potential, and linear elasticity predictions according to Eq. (13) and (14). The fact that the relaxation volumes of loops derived from simulations are larger than predictions derived from the theory of elasticity, highlights the contribution to the relaxation volumes from the highly distorted core regions at the perimeter of the loops. The contribution to the relaxation volume of dislocation loops from the core effects results in that interstitial loops appear somewhat larger, and vacancy loops somewhat smaller than what should be expected from the elasticity considerations.

The expected linear variation of elements of the dipole tensor of loops evaluated using Eq. (13) is shown in Fig. 7 and 8 together with values derived from DFT simulations. The values predicted by elasticity for the $\frac{1}{2}\langle 111\rangle$ SIA loops are lower than the DFT and MNB potential data points. It suggests the effective area of an SIA loop is slightly larger than its geometrical value expected from elasticity considerations. The values derived from DFT and atomistic simulations for vacancy loops are also larger than the values derived from elasticity. This is not unexpected as the non-linear deformations associated with the dislocation cores at the loop perimeter give an extra positive contribution to the dipole tensor and the relaxation volume of the loops.

The analysis of [001] SIA loops, where the Burgers vector points in the z direction, shows that the $P_{11} \equiv P_{xx}$ and $P_{22} \equiv P_{yy}$ elements of the dipole tensor are higher than the values predicted by linear elasticity, whereas the

$P_{33} \equiv P_{zz}$ atomistic data fluctuate around the straight line corresponding to the linear elasticity approximation.

The relaxation volumes of loops derived from atomistic simulations also differ from the elasticity predictions [54], and for the $\langle 100\rangle$ loops the difference between the DFT and atomistic values on the one hand, and elasticity predictions on the other hand, are fairly significant. This is not surprising since the core of a $\langle 100\rangle$ dislocation is characterised by strong non-linear deformations, which increase the apparent relaxation volume of the defect.

The formation energy of an open vacancy loop or a void is dominated by their surface energy and surface stress [36, 54]. We write

$$E_{surf} = \int \gamma dA, \qquad (15)$$

where γ is the surface energy density, and dA is an infinitesimal element of surface area. This integral can be
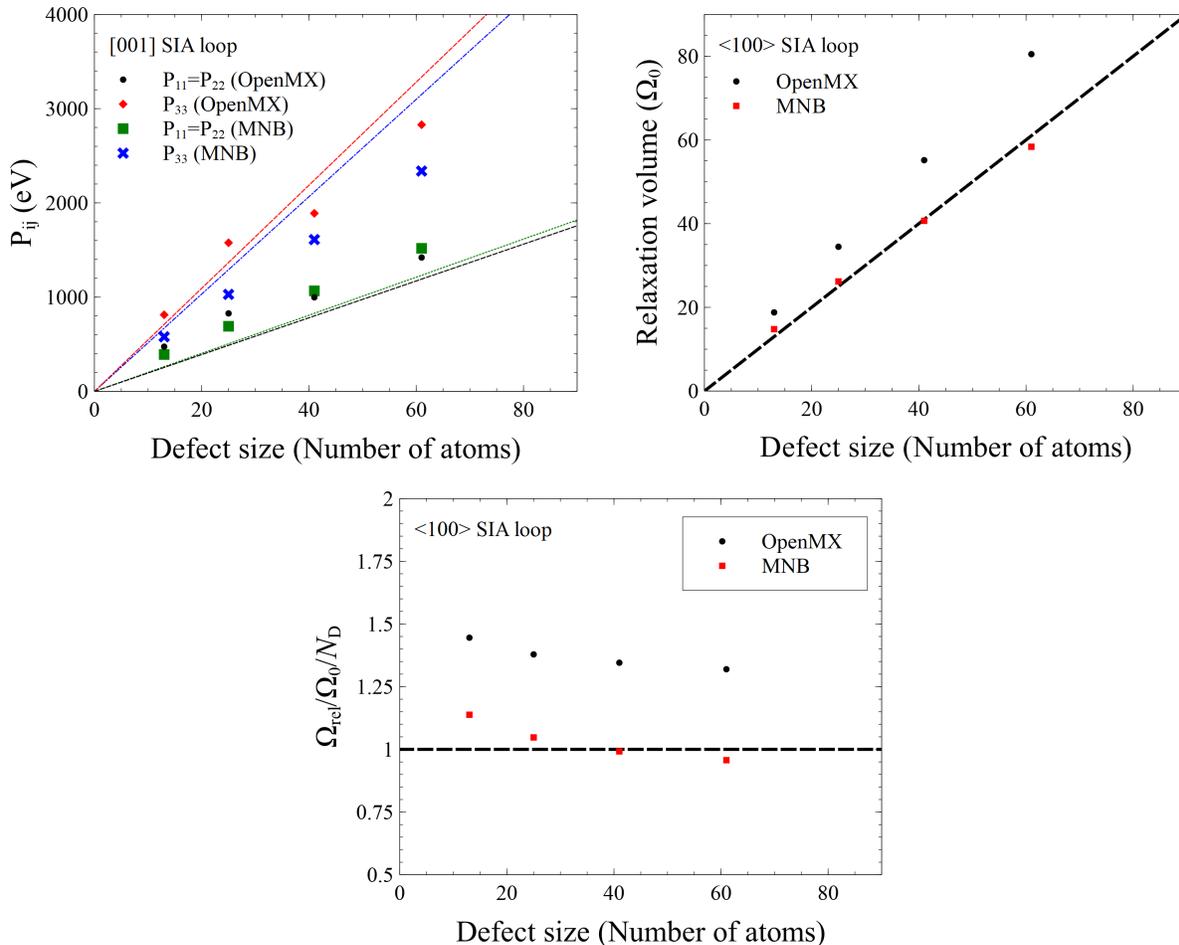
FIG. 8. Calculated elastic dipole tensor P_{ij} and relaxation volume of $\langle 100 \rangle$ SIA loops with $\mathbf{b} = [001]$ using OpenMX and MNB potential, and linear elasticity predictions according to Eqns. (13) and (14).

	degeneracy	$c_{(hkl)}$
$\{100\}$	6	0.02893824442681180
$\{110\}$	12	0.02222232701901629
$\{111\}$	8	0.01158844076701676
$\{211\}$	24	0.01945812846145005

TABLE IV. Coefficients for calculating the average surface energy of a spherical void.

approximated by a sum over surface facets

$$E_{surf} \approx \sum_{(hkl)} \gamma_{(hkl)} A_{(hkl)}, \qquad (16)$$

where $A_{(hkl)}$ is the area of an (hkl) surface.

For a spherical void, we may approximate its surface energy E_{void} as

$$A_{(hkl)} = c_{(hkl)} A_{total}, \qquad (17)$$

where coefficient $c_{(hkl)}$ equals the Voronoi area corre-

sponding to a surface normal direction on a unit sphere divided by 4π. The sum of all the $c_{(hkl)}$ is unity, and their values are listed in Table IV (see appendix A). The surface area of a spherical void $A_{total} = 4\pi r^2$. The radius r of a void can be calculated from its volume as $V = N\Omega_0 = (4/3)\pi r^3$.

Evaluating the energy of a planar void (which is an open dislocation loop) is somewhat complicated by the need to take into account the thin strip of atoms on its perimeter (see appendix A). In appendix C, we find an expression providing a good fit to the data, but we also show that it is acceptable to approximate the energy simply by considering the areas of the planar facets, as in Ref. [36]

$$E_{open} \approx 2A_{face} \gamma_{\hat{n}}, \qquad (18)$$

where $\gamma_{\hat{n}}$ is the surface energy density for a surface with normal $\hat{n}$ and A_{face} is the area of one face of the planar void. In this approximation, the energy associated with the perimeter of the open loop is ignored.

The formation energies predicted by the above approximations, together with DFT and MNB potential data,
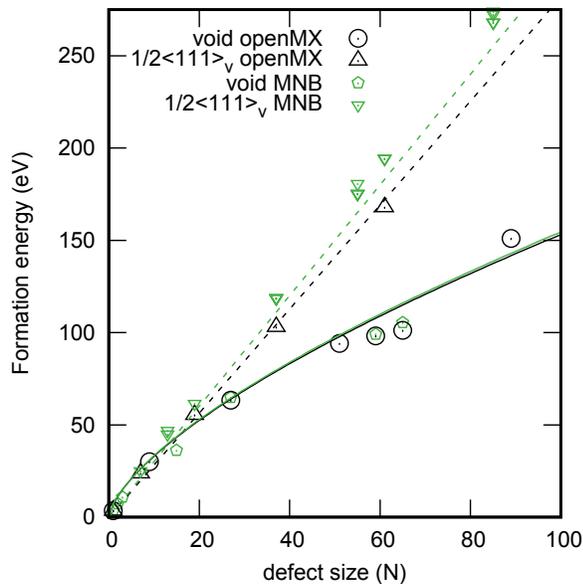
FIG. 9. Formation energies of $\frac{1}{2}\langle 111\rangle$ open vacancy loops and voids calculated using OpenMX and MNB potential, compared with values derived from Eqs. (16) and (18).

are presented in Fig. 9. From the comparison, it appears that the formulae for the formation energy of spherical and planar voids match the atomistic simulation data very well. Values of γ are presented in appendix B.

The dipole tensor of a spherical void has so far been evaluated only in the isotropic elasticity limit in the literature [54]. The relaxation volume of a void can be written as

$$\Omega_{rel} \approx -4\pi \left(\frac{1-\nu}{1-2\nu} \right) \frac{sr^2}{K}, \qquad (19)$$

where ν is the Poisson's ratio, s is the average surface stress, and K is the bulk modulus. The dipole tensor of a void only has diagonal elements. In the isotropic limit, we can write

$$P_{11} = P_{22} = P_{33} = K\Omega_{rel} = -4\pi \left(\frac{1-\nu}{1-2\nu} \right) sr^2. \quad (20)$$

The value of Poisson's ratio and bulk modulus can be obtained through $\nu = C_{12}/(C_{11} + C_{12})$ and $K = (C_{11} + 2C_{12})/3$. The definition and values of surface stress s_{ij} calculated using OpenMX and MNB potential are presented in appendix B. The average surface stress is calculated by taking the average of the eigenvalues of s_{ij} of different (hkl) surfaces on a sphere according to the coefficient $c_{(hkl)}$. We obtain $s = 0.1891 \mathrm{eV/\AA^2}$ from the OpenMX data, and $s = 0.2523 \mathrm{eV/\AA^2}$ from the MNB potential data.

In Fig. 10, we show the predicted values of diagonal elements of dipole tensor of a void according to Eq. (20) together with our data. Since the values of s differ between OpenMX data and MNB potential data, the corresponding predictions are also different. However, both suggest

good compatibility between linear elasticity theory and DFT and many-body potential. We note that tungsten is elastically nearly isotropic, and for anisotropic materials our theory will need to be adjusted.

IV. COMPARISON WITH MANY-BODY POTENTIALS

The molecular statics analysis by Gilbert et $al.$ [36], using the DND many-body potential [63], found the critical size at which a closed $1/2\langle 111\rangle$ vacancy loop in tungsten is more stable than an open vacancy loop, occurs at a diameter of 34 Å, corresponding approximately to a 157-vacancy defect. The average surface energy density γ calculated using the DND potential is 0.174 eV/Å^2. This value is smaller than the DFT result obtained using VASP, where $\gamma = 0.229$ eV/Å^2 [54]. It is expected that a DFT calculation should predict a vacancy closed loop to be more energetically favourable than an open loop (planar void) at smaller sizes, comparing to molecular statics. Similar calculations by Fikar et $al.$ [64] found a critical size of 30 vacancies for the Ackland-Thetford [65] potential and 115 vacancies for the Marinica et $al.$ EAM4 potential [66].

We can compare the formation energy per vacancy of $\frac{1}{2}\langle 111\rangle[111]$ vacancy closed loops and $\frac{1}{2}\langle 111\rangle[111]$ planar voids computed using openMX with an embedded-atom potential [53], see Fig. 11. As empirical potential relaxations are computationally inexpensive, we have sampled a broad range of competing metastable structures. We characterize an idealised circular planar void with Burgers vector parallel to its habit plane normal $\hat{\mathbf{n}}$ by its Burgers vector $\mathbf{b}$, and a single radius r. For convenience we choose the sign of $\hat{\mathbf{n}}$ such that $\hat{\mathbf{n}} \cdot \mathbf{b} > 0$. The vacancies within the defect lie within a cylinder, bounded by a circle oriented normal to $\hat{\mathbf{n}}$ with radius r, and a second similar circle translated by the vector $\mathbf{b}$. We set the radius with $V = \pi r^2 b = N\Omega_0$.

We remove atoms within this cylinder, then to close it to promote the formation of a loop we can then displace the remaining atoms separated by $\mathbf{d}$ from the centre of the defect by a vector

$$\boldsymbol{\delta} = \pm \xi \frac{\mathbf{b}}{2} \left(1 - \frac{|z|}{z_0} \right) \min\left(1, 2 - \frac{x}{r} \right), \qquad (21)$$

in the region $|z| < z_0$ and $x < 2r$, where $z = \mathbf{r} \cdot \hat{\mathbf{n}}$ is the projection along the normal, z_0 is half the simulation cell length, and $x = |\mathbf{d} - (\mathbf{d} \cdot \hat{\mathbf{b}})\hat{\mathbf{b}}|$ is the projection perpendicular to $\mathbf{b}$, where $\hat{\mathbf{b}}$ is the unit vector of $\mathbf{b}$. ξ is a scaling factor, which we set to zero to generate a planar void. Setting ξ to higher values up to 1.0 promotes the formation of a range of planar voids and vacancy loops, which may appear with different metastable core structures.

Loops with habit planes not parallel to $\mathbf{b}$ were generated similarly, but with atoms initially removed in a sheared elliptical cylinder. These are considered in
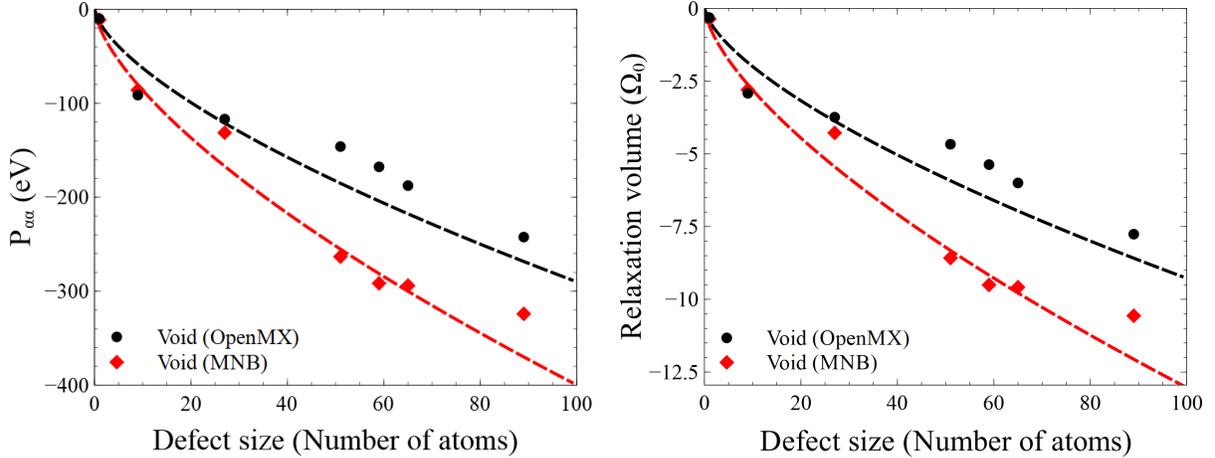
FIG. 10. Elastic dipole tensors and relaxation volumes of voids calculated using OpenMX and MNB potential, plotted together with linear elasticity predictions derived from Eqns. (20) and (19). All the off-diagonal elements of dipole tensors vanish because of symmetry considerations.
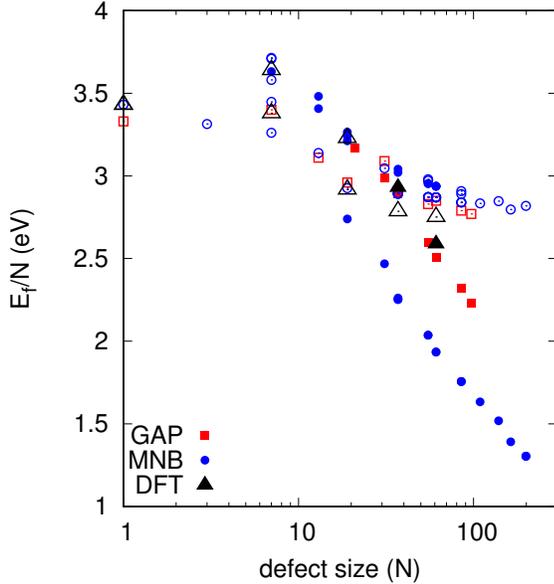
FIG. 11. The formation energy E_f per vacancy of $\frac{1}{2}\langle 111\rangle[111]$ vacancy closed loops (closed symbols) and $\frac{1}{2}\langle 111\rangle[111]$ planar voids (open symbols) computed with DFT (this work), results taken from a newly developed GAP potential in Ref. [55], and the empirical embedded-atom MNB potential [53]. Note that the MNB potential has a higher vacancy formation energy than the other two, so has been shifted down by 0.3eV.

more detail in appendix C. We have only found stable $\mathbf{b} = a_0/2\langle 111\rangle$ vacancy loops on a [111] normal habit plane. If initiated on other planes, they shear back to a [111] normal or do not remain closed. $\mathbf{b} = a_0\langle 100\rangle$ loops were found to be stable on [100] and [211] habit planes, with the latter being lower in energy. We could not find $\mathbf{b} = a_0\langle 110\rangle$ loops on any habit plane, attempts either

formed planar voids or split into multiple $1/2\langle 111\rangle$ and $\langle 100\rangle$ segments.

The identification of the defect nature as loop or planar void was performed using the DXA analysis [67] after relaxation.

We also compare with results taken from a recently developed GAP potential [55]. The MNB potential was developed comparing to the AM05 DFT functional, and has a higher vacancy formation energy than the OpenMX vacancy formation energy, 3.74eV compared to 3.428 eV. If we take this into account by shifting the energy for these empirical results by -0.3eV, so that the vacancy formation energies coincide, three distinct branches of $1/2\langle 111\rangle$ vacancy defects emerge. The energy per vacancy in a planar void coincides for all the three methods, appearing to plateau just under 3 eV. The energy per vacancy of a vacancy loop has an upper and a lower branch. The upper branch shows well-matched results for all three methods, showing a formation energy decreasing as $\sqrt{N}\ln N$. The lower branch is only occupied by the MNB empirical potential, and appears to show a different dislocation core structure. The fact that low energy structures appear on this branch for the empirical potential at loop sizes $N = 20 - 40$ is most probably a failure of the empirical potential to reproduce the correct core at these sizes.

We have further information about these branches of structures from their relaxation volumes, shown in figure 12. We see the upper branch, corresponding to planar voids, coinciding for both DFT and empirical potentials, with a small relaxation volume per point defect. The bottom branch shows well-resolved $1/2\langle 111\rangle[111]$ vacancy loops, with a relaxation volume of (minus) one atomic volume per vacancy in the defect. This is the expected relaxation volume per vacancy in the infinite loop size limit. The middle branch shows $1/2\langle 111\rangle[111]$ vacancy loops, which at larger sizes DXA analysis identifies as having a Burgers vector $b = a_0/2\langle 111\rangle$, but with
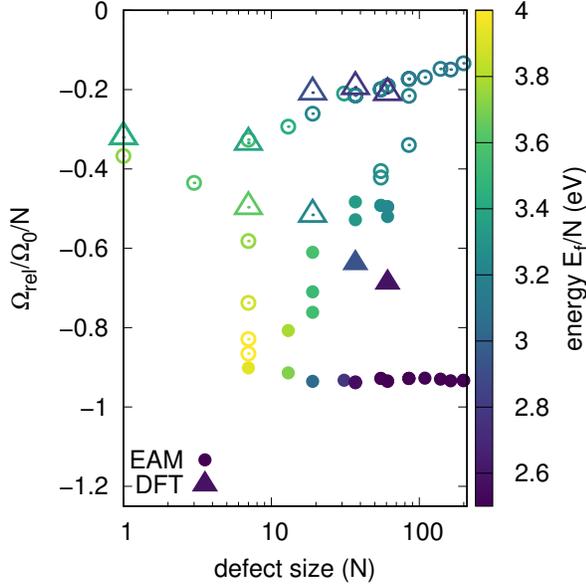
FIG. 12. The relaxation volume per vacancy of $1/2\langle111\rangle[111]$ vacancy loops (closed symbols) and $1/2\langle111\rangle[111]$ planar voids (open symbols) computed with DFT (this work) and the empirical embedded-atom MNB potential [53]. Points are coloured by formation energy per point defect.

a smaller relaxation volume per vacancy. It is unclear whether the low branch is an erroneous prediction.

Our results at present suggest our DFT data on mesoscopic loops are not yet reaching the macrosopic limit where linear elasticity applies. One the other hand, our data complements where the linear elasticity approximation fails.

V. CONCLUSIONS

We have evaluated the dipole tensors and formation energies of $\frac{1}{2}\langle111\rangle$ SIA, closed and open vacancy loops, $\langle100\rangle$ SIA loops and spherical voids using large scale density function theory calculations. The results compare well with elasticity and molecular statics calculations and show good transferability to larger scale continuum models.

The data enable deriving interpolations for the formation energy of micro- and mesoscopic defects, as well as for the dipole tensors of the defects entering the general equation for the energy of an ensemble of interacting defects

$$E_{\text{total}}^{F} = \sum_{a} E_{a}^{F} + \frac{1}{2}\sum_{a,b} P_{ij}^{a}\frac{\partial^2 G_{ik}(\mathbf{R}_{ab})}{\partial x_j \partial x_l}P_{kl}^{b} - \sum_{a} P_{ij}^{a}\epsilon_{ij}^{ext},$$
$$(22)$$

where $\mathbf{R}_{ab}$ is the separation between defects a and b, G_{ij} is the elastic Green's function and ϵ_{ij}^{ext} is the strain tensor of external elastic field.

Analysis of vacancy loops using molecular statics suggests that there are intermediate metastable configurations between open and closed loops. Although the linear elasticity approximation compares well with our DFT data, it appears that the configuration and the formation energy of open and closed vacancy loops might not be unique, particularly on the mesoscopic scale where the core effects play a significant part.

Appendix A: Surface area of voids and open loops

We take the approximation that the surface of a void is composed of facets of {100}, {110}, {111} and {211} surfaces. There are totally 50 different orientations. The area of each facet is calculated according to the Voronoi area around the point of a surface normal vector on a unit sphere in spherical geometry. The area $A_{(hkl)}$ corresponding to the (hkl) surface is normalized by 4π, which gives the coefficient $c_{(hkl)}$. Their values are in table IV.

In the case of an open loop (or planar void), if we consider it resembles a cylinder, the top and bottom surface is determined by its habit plane. We also need to calculate the contribution along its perimeter. The contribution of different surfaces along its perimeter may be obtained by calculating the length of the intersection of a unit circle on each facet of the unit sphere, where the normal vector of the plane that the unit circle is in is along the Burgers vector of the loop. The length of the intersection is then normalized by 2π, which gives the coefficient $d_{(hkl)}$. In the case of a $\frac{1}{2}\langle111\rangle$ open loop, we can obtain,

$$d_{(\bar{1}10)} = d_{(\bar{1}01)} = d_{(0\bar{1}1)} = d_{(1\bar{1}0)} = d_{(10\bar{1})} = d_{(01\bar{1})}$$
$$= d_{(\bar{2}11)} = d_{(1\bar{2}1)} = d_{(11\bar{2})} = d_{(2\bar{1}\bar{1})} = d_{(\bar{1}2\bar{1})} = d_{(\bar{1}\bar{1}2)}$$
$$= 1/12. \qquad (A1)$$

In the case of a $\langle100\rangle$ open loop, we can obtain,

$$d_{(010)} = d_{(001)} = d_{(0\bar{1}0)} = d_{(00\bar{1})}$$
$$= d_{(011)} = d_{(0\bar{1}1)} = d_{(01\bar{1})} = d_{(0\bar{1}\bar{1})} = 1/8. \quad (A2)$$

Other unlisted values are all zeros.

Appendix B: Surface energy density and surface stress from DFT calculations

We calculated the surface energy density and surface stress of {100}, {110}, {111} and {211} surfaces using OpenMX, and also compared them with data calculated by molecular statics using MNB potential [53].

Firstly, we relax simulation boxes of perfect lattice to stress free condition. In the calculation of a (001) surface, we used a unit cell with $\mathbf{a}_1 = [100]$, $\mathbf{a}_2 = [010]$, and $\mathbf{a}_3 = [001]$ containing 2 atoms. In the calculation of other surfaces, i.e. $(10\bar{1})$, (111), $(\bar{1}2\bar{1})$, we used a unit cell with $\mathbf{a}_1 = [10\bar{1}]$, $\mathbf{a}_2 = [\bar{1}2\bar{1}]$, and $\mathbf{a}_3 = [111]/2$ containing 6

atoms. Details of different box sizes and k-points are listed in table V.

Then, we fixed the box shape and removed half of the atoms along the surface direction creating the decided surfaces. The surface energy density can be obtained as

$$\gamma_{(hkl)} = \frac{1}{2A}\left(E_{2s} - \frac{N_{2s}}{N_{perf}}E_{perf}\right), \qquad (B1)$$

where A is the area of a surface, E_{2s} is the energy of the box having 2 surfaces, E_{perf} is the total energy of the relaxed perfect lattice box, N_{2s} is the number of atoms of the box with 2 surfaces and N_{perf} is the total number of atoms of the relaxed perfect lattice box. The factor of 2 comes from the top and bottom surfaces. Calculated values are presented in Table V.

The surface stress can be written as [68]:

$$s_{ij} = \frac{1}{A}\frac{\partial(\gamma A)}{\partial\epsilon_{ij}} = \frac{1}{2A}\frac{\partial E_{2s}}{\partial\epsilon_{ij}} = \frac{1}{2A}V_{box}\bar{\sigma}_{ij} \qquad (B2)$$

where $\bar{\sigma}_{ij}$ is the stress of the simulation box with surfaces. It allows us to obtain s_{ij} directly from the same DFT calculation. Besides, we can rewrite the right hand side according to chain rule:

$$s_{ij} = \frac{1}{A}\frac{\partial(\gamma A)}{\partial\epsilon_{ij}} = \frac{\gamma}{A}\frac{\partial A}{\partial\epsilon_{ij}} + \frac{\partial\gamma}{\partial\epsilon_{ij}}. \qquad (B3)$$

Assuming a surface with a unit normal vector in the z direction, and the surface is on $x - y$ plane, one can derive

$$\frac{1}{A}\frac{\partial A}{\partial\boldsymbol{\epsilon}} = \begin{pmatrix} 1 & 0 & 0 \\ 0 & 1 & 0 \\ 0 & 0 & 0 \end{pmatrix}. \qquad (B4)$$

Generally, if the unit normal vector $\hat{\mathbf{n}} = (n_x, n_y, n_z)$ is in an arbitrary direction, one can derive:

$$\frac{1}{A}\frac{\partial A}{\partial\epsilon_{ij}} = \delta_{ij} - n_i n_j \qquad (B5)$$

This gives the derivative of a small flat area in an arbitrary direction.

Then, we can also obtain the derivative of the surface energy density with respect to strain $\partial\gamma/\partial\boldsymbol{\epsilon}$. Raw data of s_{ij} and $\partial\gamma/\partial\boldsymbol{\epsilon}$ in the simulation box coordinate are presented in table VI and VII. We adjusted OpenMX data according to the symmetry that we can observe in MND potential data, and rotate them in the [100],[010],[001] coordinate. These data are presented in table VIII and IX.

Appendix C: Formation energy of a planar void with arbitrary normal

We characterize an idealised planar void (or open loop) by its Burgers vector $\mathbf{b}$, the unit vector normal to its

	L_1	L_2	L_3	k_1	k_2	k_3	γ (MNB)	γ (OpenMX)
(001)	1	1	40	21	21	3	0.2397	0.2591
$(10\bar{1})$	28	1	1	3	9	25	0.2182	0.2115
(111)	1	1	46	15	9	3	0.2594	0.2385
$(\bar{1}2\bar{1})$	1	16	1	15	3	25	0.2413	0.2236
mean							0.235	0.228

TABLE V. Details of different box sizes and k-points, and the surface energy density γ. L_1, L_2 and L_3 are the box lengths in the unit of unit cell. In the calculation of (100) surface, we used a unit cell with $\mathbf{a}_1 = [100]$, $\mathbf{a}_2 = [010]$, and $\mathbf{a}_3 = [001]$ containing 2 atoms. In the calculation of other surfaces, we used a unit cell with $\mathbf{a}_1 = [10\bar{1}]$, $\mathbf{a}_2 = [\bar{1}2\bar{1}]$, and $\mathbf{a}_3 = [111]/2$ containing 6 atoms. Unit cell vectors are in units of lattice constant. k_1, k_2 and k_3 are the k-point mesh being used. γ is in unit of ev/Å^2.

MNB	s_{11}	s_{22}	s_{33}	s_{12}	s_{23}	s_{31}
(001)	0.2294	0.2294	0.0000	0.0000	0.0000	0.0000
$(10\bar{1})$	0.0000	0.2917	0.2535	0.0000	0.0541	0.0000
(111)	0.2145	0.2145	0.0000	0.0000	0.0000	0.0000
$(\bar{1}2\bar{1})$	0.2621	0.0000	0.2514	0.0000	0.0000	0.0000
OpenMX	s_{11}	s_{22}	s_{33}	s_{12}	s_{23}	s_{31}
(001)	0.1468	0.1468	-0.0117	0.0000	0.0000	0.0000
$(10\bar{1})$	0.0081	0.2575	0.2214	0.0000	0.0587	0.0000
(111)	0.1347	0.1345	0.0015	0.0000	0.0184	0.0000
$(\bar{1}2\bar{1})$	0.1514	-0.0001	0.2225	-0.0010	-0.0236	0.0000

TABLE VI. Surface stress calculated using OpenMX and MNB potential. They are in the unit of eV/Å^2. They are presented in the original coordinate system.

habit plane $\hat{\mathbf{n}}$, and a single radius r. For convenience we will choose the sign of $\hat{\mathbf{n}}$ such that $\hat{\mathbf{n}} \cdot \mathbf{b} > 0$, and write $\hat{\mathbf{b}} = \mathbf{b}/b$. The vacancies within the defect lie within a sheared elliptical cylinder, bounded by ellipse oriented normal to $\hat{\mathbf{n}}$ with minor and major radii r and r/ζ, where $\zeta = \hat{\mathbf{b}} \cdot \hat{\mathbf{n}} \leq 1$, and a second similar ellipse translated by the vector $\zeta\hat{\mathbf{b}}$. In the case $\hat{\mathbf{n}} \parallel \mathbf{b}$, this reduces to a regular circular cylinder with $\zeta = 1$. The volume V is invariant to shear, so we set the radius with $V = \pi r^2 b = N\Omega_0$.

The energy of a planar void should have contributions from the elliptical faces and the perimeter strip,

$$E_{open} = 2A_{face}\gamma_{\hat{\mathbf{n}}} + A_{peri}\gamma_{peri}. \qquad (C1)$$

As the perimeter strip is a sheared elliptical cylinder, its area is non-trivial, but in practice it is not a good estimator of the true area anyway. We can compute the surface area of unrelaxed planar voids in a bcc material using qhull [69], assuming each vacancy is surrounded by a shell of points in the family $a_0[0\,^1/_4\,^1/_2]$. The area of the face is $A_{face} = 2\pi r^2/\zeta$. The area of the perimeter strip can be estimated using the Ramanujan formula perimeter
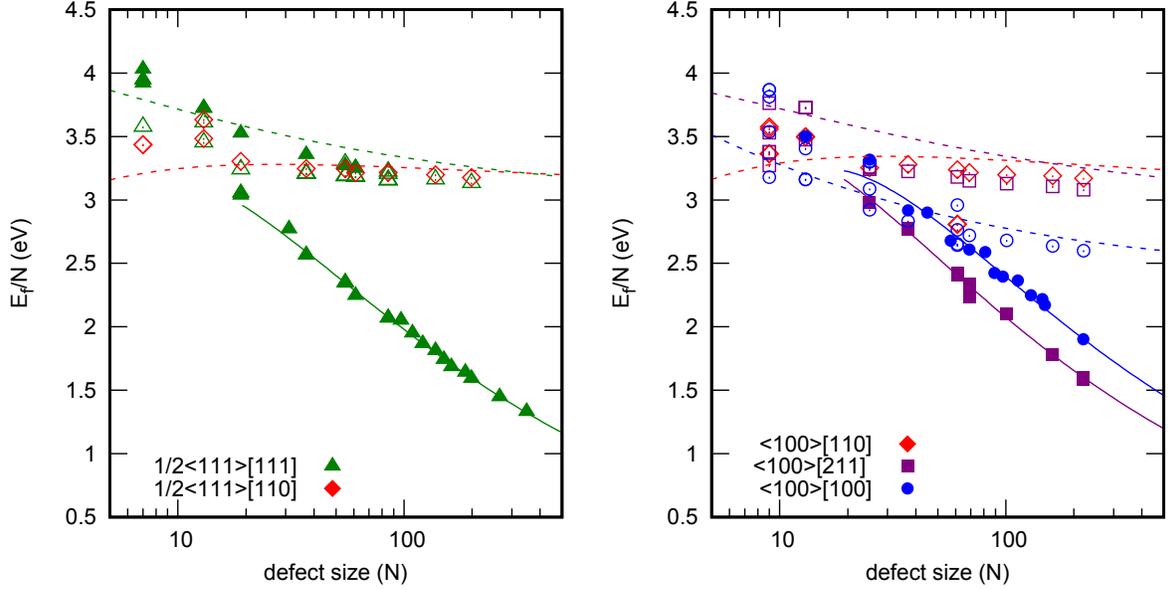
FIG. 13. Formation energy of vacancy defects computed with the MNB potential. Dislocation loops, determined using DXA, are shown as closed symbols, and planar voids as open symbols. Solid lines are empirical fits to dislocation loop energy (see table III) and dashed lines use the loop geometry and surface energy only (equation C3).

MNB	$\partial\gamma/\partial\epsilon_{11}$	$\partial\gamma/\partial\epsilon_{22}$	$\partial\gamma/\partial\epsilon_{33}$	$\partial\gamma/\partial\epsilon_{12}$	$\partial\gamma/\partial\epsilon_{23}$	$\partial\gamma/\partial\epsilon_{31}$
(001)	-0.0103	-0.0103	0.0000	0.0000	0.0000	0.0000
$(10\bar{1})$	0.0000	0.0735	0.0352	0.0000	0.0541	0.0000
(111)	-0.0449	-0.0449	0.0000	0.0000	0.0000	0.0000
$(\bar{1}2\bar{1})$	0.0208	0.0000	0.0102	0.0000	0.0000	0.0000
OpenMX	$\partial\gamma/\partial\epsilon_{11}$	$\partial\gamma/\partial\epsilon_{22}$	$\partial\gamma/\partial\epsilon_{33}$	$\partial\gamma/\partial\epsilon_{12}$	$\partial\gamma/\partial\epsilon_{23}$	$\partial\gamma/\partial\epsilon_{31}$
(001)	-0.1123	-0.1123	-0.0117	0.0000	0.0000	0.0000
$(10\bar{1})$	0.0081	0.0460	0.0100	0.0000	0.0587	0.0000
(111)	-0.1038	-0.1040	0.0015	0.0000	0.0184	0.0000
$(\bar{1}2\bar{1})$	-0.0722	-0.0001	-0.0010	-0.0010	-0.0236	0.0000

TABLE VII. The derivative of surface energy density with respect to strain calculated using OpenMX and MNB potential. They are in the unit of eV/Å^2. They are presented in the original coordinate system.

MNB	s_{11}	s_{22}	s_{33}	s_{12}	s_{23}	s_{31}
(001)	0.2294	0.2294	0.0000	0.0000	0.0000	0.0000
$(10\bar{1})$	0.1076	0.3300	0.1076	0.0000	0.0000	0.1076
(111)	0.1430	0.1430	0.1430	-0.0715	-0.0715	-0.0715
$(\bar{1}2\bar{1})$	0.2149	0.0838	0.2149	0.0838	0.0838	-0.0472
OpenMX	s_{11}	s_{22}	s_{33}	s_{12}	s_{23}	s_{31}
(001)	0.1468	0.1468	0.0000	0.0000	0.0000	0.0000
$(10\bar{1})$	0.0891	0.3008	0.0891	0.0000	0.0000	0.0891
(111)	0.0897	0.0897	0.0897	-0.0449	-0.0449	-0.0449
$(\bar{1}2\bar{1})$	0.1499	0.0742	0.1499	0.0742	0.0742	-0.0015

TABLE VIII. Surface stress calculated using OpenMX and MNB potential. They are in the unit of eV/Å^2. They are adjusted according to symmetry observed and rotated to [100], [010], [001] coordinate system.

length p,

$$p \simeq \pi r \left((3 + 3/\zeta) - \sqrt{(3 + 1/\zeta)(1 + 3/\zeta)} \right), \quad \text{(C2)}$$

giving $A_{\mathrm{peri}} \simeq p\zeta b$.

If we write the surface area as the elliptical surfaces plus a variable effective contribution from the perimeter strip, i.e. $A = 2A_{\mathrm{face}} + \lambda A_{\mathrm{peri}}$, we can find the effective contribution λ. The result is shown in figure 14. At small defect sizes, λ is small, indicating that a good estimate for the surface area is the elliptical surfaces alone. At large defect sizes, λ increases with $\log N$, and shows no convergence at large size. This is a consequence of the discrete atomic nature of the defect boundary and a manifestation of the Schwarz lantern problem [70]: it is

not possible to approximate the surface area of a smooth curved surface using triangles with fixed normals.

To solve for λ analytically would require a solution of the well-known Gauss circle problem, so instead we provide fits of the empirical form $\lambda(N) = \alpha \log N + \beta$ in table X. The energy of the elliptical planar void should then be, to a good approximation,

$$E_{\mathrm{open}} = \frac{2\pi r^2}{\zeta} \gamma_{\hat{\mathbf{n}}} + \lambda p \zeta b \bar{\gamma}, \quad \text{(C3)}$$

where $\bar{\gamma}$ is an average surface energy. The energy of planar voids and dislocation loops computed with the MNB potential are shown in figure 13, showing a very high quality agreement.

MNB	$\partial\gamma/\partial\epsilon_{11}$	$\partial\gamma/\partial\epsilon_{22}$	$\partial\gamma/\partial\epsilon_{33}$	$\partial\gamma/\partial\epsilon_{12}$	$\partial\gamma/\partial\epsilon_{23}$	$\partial\gamma/\partial\epsilon_{31}$
(001)	-0.0103	-0.0103	0.0000	0.0000	0.0000	0.0000
(10$\bar{1}$)	-0.0015	0.1117	-0.0015	0.0000	0.0000	-0.0015
(111)	-0.0299	-0.0299	-0.0299	0.0150	0.0150	0.0150
($\bar{1}$2$\bar{1}$)	0.0138	0.0034	0.0138	0.0034	0.0034	-0.0070
OpenMX	$\partial\gamma/\partial\epsilon_{11}$	$\partial\gamma/\partial\epsilon_{22}$	$\partial\gamma/\partial\epsilon_{33}$	$\partial\gamma/\partial\epsilon_{12}$	$\partial\gamma/\partial\epsilon_{23}$	$\partial\gamma/\partial\epsilon_{31}$
(001)	-0.1123	-0.1123	0.0000	0.0000	0.0000	0.0000
(10$\bar{1}$)	-0.0167	0.0893	-0.0167	0.0000	0.0000	-0.0167
(111)	-0.0693	-0.0693	-0.0693	0.0346	0.0346	0.0346
($\bar{1}$2$\bar{1}$)	-0.0365	-0.0003	-0.0365	-0.0003	-0.0003	0.0358

TABLE IX. The derivative of surface energy density with respect to strain calculated using OpenMX and MNB potential. They are in the unit of eV/Å^2. They are adjusted according to symmetry observed and rotated to [100], [010], [001] coordinate system.
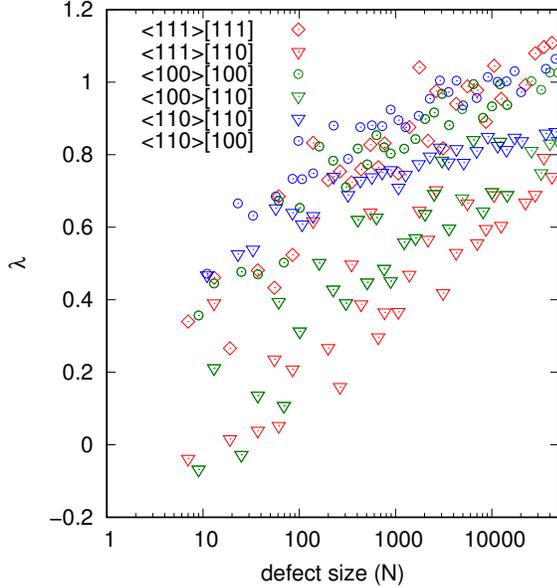
FIG. 14. Calculated surface area correction for a planar void due to the perimeter strip. The surface area measure by qhull is $A = 2\pi r^2/\zeta + \lambda p\zeta b$, where p is the perimeter length.

At small planar void sizes we note that λ is small, sug-

gesting that the perimeter strip effective area is smaller than expected, and we may be able to neglect it. At large planar void sizes the perimeter strip area scales as $\sqrt{N}$, and so is small compared to the surface area (scaling as N). It is not, therefore, unreasonable to neglect the perimeter strip in all cases, and just use

$$E_{\text{open}} \approx \frac{2\pi r^2}{\zeta}\,\gamma_{\hat{\mathbf{n}}}, \qquad (C4)$$

where r is a function of N. This is the justification for our use of equation 16 in the main text.

b	n	α	β
$\frac{1}{2}\langle 111\rangle$	[111]	0.0859	0.215
$\frac{1}{2}\langle 111\rangle$	[110]	0.0813	-0.107
$\langle 100\rangle$	[100]	0.0718	0.307
$\langle 100\rangle$	[110]	0.0955	-0.132
$\langle 100\rangle$	[211]	0.0949	0.148
$\langle 110\rangle$	[110]	0.0421	0.440
$\langle 110\rangle$	[100]	0.0560	0.482
$\langle 110\rangle$	[211]	0.0584	0.465

TABLE X. Fitted estimates for the effective contribution λ to a planar void surface area from the perimeter strip, $A = 2\pi r^2/\zeta + \lambda p\zeta b$, where p is the perimeter length estimated by Ramanujan formula, eqn C2. These values are fits of the form $\lambda(N) = \alpha \log N + \beta$ to the points in figure 14. Note that these values are for unrelaxed planar voids in a bcc metal, and are not material specific.

ACKNOWLEDGMENTS

[1] J.H. You, E. Visca, Ch. Bachmann, T. Barrett, F. Crescenzi, M. Fursdon, H. Greuner, D. Guilhem, P. Languille, M. Li, S. McIntosh, A.V. Mller, J. Reiser, M. Richou, and M. Rieth, "European DEMO divertor target: Operational requirements and material-design interface," **9**, 171–176 (2016).

[2] A. J. H. Donné and William Morris, *European Research Roadmap to the Realisation of Fusion Energy* (EUROfusion, 2018).

[3] T. Hirai, S. Panayotis, V. Barabash, C. Amzallag, F. Escourbiac, A. Durocher, M. Merola, J. Linke, Th. Loewenhoff, G. Pintsuk, M. Wirtz, and I. Uytdenhouwen, "Use of tungsten material for the ITER divertor," Nuclear Materials and Energy **9**, 616–622 (2016).

[4] M.R. Gilbert and J.-Ch. Sublet, "Neutron-induced transmutation effects in w and w-alloys in a fusion environment," Nuclear Fusion **51**, 043005 (2011).

[5] A. E. Sand, S. L. Dudarev, and K. Nordlund, "High-

energy collision cascades in tungsten: Dislocation loops structure and clustering scaling laws," EPL (Europhysics Letters) **103**, 46003 (2013).

[6] A.E. Sand, K. Nordlund, and S.L. Dudarev, "Radiation damage production in massive cascades initiated by fusion neutrons in tungsten," Journal of Nuclear Materials **455**, 207 – 211 (2014), proceedings of the 16th International Conference on Fusion Reactor Materials (ICFRM-16).

[7] A. E. Sand, M. J. Aliaga, M. J. Caturla, and K. Nordlund, "Surface effects and statistical laws of defects in primary radiation damage: Tungsten vs. iron," EPL (Europhysics Letters) **115**, 36001 (2016).

[8] A. E. Sand, D. R. Mason, A. De Backer, X. Yi, S. L. Dudarev, and K. Nordlund, "Cascade fragmentation: deviation from power law in primary radiation damage," Materials Research Letters **5**, 357–363 (2017).

[9] D.R. Mason, A.E. Sand, X. Yi, and S.L. Dudarev, "Direct observation of the spatial distribution of primary cascade damage in tungsten," Acta Materialia **144**, 905 – 917 (2018).

[10] X. Yi, A. E. Sand, D. R. Mason, M. A. Kirk, S. G. Roberts, K. Nordlund, and S. L. Dudarev, "Direct observation of size scaling and elastic interaction between nano-scale defects in collision cascades," EPL (Europhysics Letters) **110**, 36001 (2015).

[11] R. Alexander, M.-C. Marinica, L. Proville, F. Willaime, K. Arakawa, M. R. Gilbert, and S. L. Dudarev, "Ab initio scaling laws for the formation energy of nanosized interstitial defect clusters in iron, tungsten, and vanadium," Phys. Rev. B **94**, 024103 (2016).

[12] F. Hofmann, D. R. Mason, J. K. Eliason, A. A. Maznev, K. A. Nelson, and S. L. Dudarev, "Non-contact measurement of thermal diffusivity in ion-implanted nuclear materials," Scientific Reports **5** (2015).

[13] M. Durrand-Charre, *Microstructure of Steels and Cast Irons* (Springer-Verlag, Berlin, 2003).

[14] D R Mason, X Yi, M A Kirk, and S L Dudarev, "Elastic trapping of dislocation loops in cascades in ion-irradiated tungsten foils," Journal of Physics: Condensed Matter **26**, 375701 (2014).

[15] Xiaoou Yi, Michael L. Jenkins, Khalid Hattar, Philip D. Edmondson, and Steve G. Roberts, "Characterisation of radiation damage in W and W-based alloys from 2 MeV self-ion near-bulk implantations," Acta Materialia **92**, 163 – 177 (2015).

[16] Xiaoou Yi, Michael L. Jenkins, Marquis A. Kirk, Zhongfu Zhou, and Steven G. Roberts, "In-situ TEM studies of 150 kev W+ ion irradiated W and W-alloys: Damage production and microstructural evolution," Acta Materialia **112**, 105 – 120 (2016).

[17] X. Yi, M.L. Jenkins, M. Briceno, S.G. Roberts, Z. Zhou, and M.A. Kirk, "In situ study of self-ion irradiation damage in w and w5re at 500c," Philosophical Magazine **93**, 1715–1738 (2013).

[18] Francesco Ferroni, Xiaoou Yi, Kazuto Arakawa, Steven P. Fitzgerald, Philip D. Edmondson, and Steve G. Roberts, "High temperature annealing of ion irradiated tungsten," Acta Materialia **90**, 380 – 393 (2015).

[19] A. Hasegawa, M. Fukuda, S. Nogami, and K. Yabuuchi, "Neutron irradiation effects on tungsten materials," Fusion Engineering and Design **89**, 1568–1572 (2014).

[20] B. C. Larson, "Historical perspective on diffraction line-profile analyses for crystals containing defect clusters,"

Crystals **9**, 257 (2019).

[21] S. L. Dudarev and Pui-Wai Ma, "Elastic fields, dipole tensors, and interaction between self-interstitial atom defects in bcc transition metals," Phys. Rev. Materials **2**, 033602 (2018).

[22] Sergei L. Dudarev, Daniel R. Mason, Edmund Tarleton, Pui-Wai Ma, and Andrea E. Sand, "A multi-scale model for stresses, strains and swelling of reactor components under irradiation," Nuclear Fusion **58**, 126002 (2018).

[23] S. L. Dudarev, M. R. Gilbert, K. Arakawa, H. Mori, Z. Yao, M. L. Jenkins, and P. M. Derlet, "Langevin model for real-time brownian dynamics of interacting nanodefects in irradiated metals," Phys. Rev. B **81**, 224107 (2010).

[24] S.L. Dudarev, K. Arakawa, X. Yi, Z. Yao, M.L. Jenkins, M.R. Gilbert, and P.M. Derlet, "Spatial ordering of nano-dislocation loops in ion-irradiated materials," Journal of Nuclear Materials **455**, 16 – 20 (2014), proceedings of the 16th International Conference on Fusion Reactor Materials (ICFRM-16).

[25] Y. Li, M. Boleininger, C. Robertson, L. Dupuy, and S. L. Dudarev, "Diffusion and interaction of prismatic dislocation loops simulated by stochastic discrete dislocation dynamics," Physical Review Materials **3**, 073805 (2019).

[26] Jan Fikar, Roman Grger, and Robin Schublin, "Effect of orientation of prismatic dislocation loops on interaction with free surfaces in bcc iron," Journal of Nuclear Materials **497**, 161 – 165 (2017).

[27] Jan Fikar, Roman Grger, and Robin Schublin, "Interaction of irradiation-induced prismatic dislocation loops with free surfaces in tungsten," Nuclear Instruments and Methods in Physics Research Section B: Beam Interactions with Materials and Atoms **393**, 186 – 189 (2017), computer Simulation of Radiation effects in Solids Proceedings of the 13 COSIRES Loughborough, UK, June 19-24 2016.

[28] E. Clouet, S. Garruchet, H. Nguyen, M. Perez, and C. S. Becquart, "Dislocation interaction with C in α-Fe: A comparison between atomic simulations and elasticity theory," Acta Materialia **56**, 3450 – 3460 (2008).

[29] Céline Varvenne, Fabien Bruneval, Mihai-Cosmin Marinica, and Emmanuel Clouet, "Point defect modeling in materials: Coupling ab initio and elasticity approaches," Phys. Rev. B **88**, 134102 (2013).

[30] Céline Varvenne and Emmanuel Clouet, "Elastic dipoles of point defects from atomistic simulations," Phys. Rev. B **96**, 224103 (2017).

[31] Pui-Wai Ma and S. L. Dudarev, "Universality of point defect structure in body-centered cubic metals," Phys. Rev. Materials **3**, 013605 (2019).

[32] Pui-Wai Ma and S. L. Dudarev, "Symmetry-broken self-interstitial defects in chromium, molybdenum, and tungsten," Phys. Rev. Materials **3**, 043606 (2019).

[33] Pui-Wai Ma and S. L. Dudarev, "Effect of stress on vacancy formation and migration in body-centered-cubic metals," Phys. Rev. Materials **3**, 063601 (2019).

[34] Pui-Wai Ma and S.L. Dudarev, "Calanie: Anisotropic elastic correction to the total energy, to mitigate the effect of periodic boundary conditions," Computer Physics Communications , 107130 (2019).

[35] G. Leibfried and N. Breuer, *Point Defects in Metals* (Springer, Berlin, 1978).

[36] M R Gilbert, S L Dudarev, P M Derlet, and D G Pettifor,

"Structure and metastability of mesoscopic vacancy and interstitial loop defects in iron and tungsten," Journal of Physics: Condensed Matter **20**, 345214 (2008).

[37] N.W. Phillips, H. Yu, S. Das, D. Yang, K. Mizohata, W. Liu, R. Xu, R.J. Harder, and F. Hofmann, "Nanoscale lattice strains in self-ion implanted tungsten," Acta Materialia **195**, 219 – 228 (2020).

[38] D R Mason, A E Sand, and S L Dudarev, "Atomistic-object kinetic monte carlo simulations of irradiation damage in tungsten," Modelling and Simulation in Materials Science and Engineering **27**, 055003 (2019).

[39] T. Ozaki, "Variationally optimized atomic orbitals for large-scale electronic structures," Phys. Rev. B **67**, 155108 (2003).

[40] T. Ozaki and H. Kino, "Numerical atomic basis orbitals from h to kr," Phys. Rev. B **69**, 195113 (2004).

[41] T. Ozaki and H. Kino, "Efficient projector expansion for the ab initio lcao method," Phys. Rev. B **72**, 045121 (2005).

[42] Kurt Lejaeghere, Gustav Bihlmayer, Torbjörn Björkman, Peter Blaha, Stefan Blügel, Volker Blum, Damien Caliste, Ivano E. Castelli, Stewart J. Clark, Andrea Dal Corso, Stefano de Gironcoli, Thierry Deutsch, John Kay Dewhurst, Igor Di Marco, Claudia Draxl, Marcin Dułak, Olle Eriksson, José A. Flores-Livas, Kevin F. Garrity, Luigi Genovese, Paolo Giannozzi, Matteo Giantomassi, Stefan Goedecker, Xavier Gonze, Oscar Grånäs, E. K. U. Gross, Andris Gulans, François Gygi, D. R. Hamann, Phil J. Hasnip, N. A. W. Holzwarth, Diana Iuşan, Dominik B. Jochym, François Jollet, Daniel Jones, Georg Kresse, Klaus Koepernik, Emine Küçükbenli, Yaroslav O. Kvashnin, Inka L. M. Locht, Sven Lubeck, Martijn Marsman, Nicola Marzari, Ulrike Nitzsche, Lars Nordström, Taisuke Ozaki, Lorenzo Paulatto, Chris J. Pickard, Ward Poelmans, Matt I. J. Probert, Keith Refson, Manuel Richter, Gian-Marco Rignanese, Santanu Saha, Matthias Scheffler, Martin Schlipf, Karlheinz Schwarz, Sangeeta Sharma, Francesca Tavazza, Patrik Thunström, Alexandre Tkatchenko, Marc Torrent, David Vanderbilt, Michiel J. van Setten, Veronique Van Speybroeck, John M. Wills, Jonathan R. Yates, Guo-Xu Zhang, and Stefaan Cottenier, "Reproducibility in density functional theory calculations of solids," Science **351** (2016), 10.1126/science.aad3000, https://science.sciencemag.org/content/351/6280/aad3000.full.pdf.

[43] G. B. Bachelet, D. R. Hamann, and M. Schlüter, "Pseudopotentials that work: From h to pu," Phys. Rev. B **26**, 4199–4228 (1982).

[44] N. Troullier and José Luís Martins, "Efficient pseudopotentials for plane-wave calculations," Phys. Rev. B **43**, 1993–2006 (1991).

[45] Leonard Kleinman and D. M. Bylander, "Efficacious form for model pseudopotentials," Phys. Rev. Lett. **48**, 1425–1428 (1982).

[46] Peter E. Blöchl, "Generalized separable potentials for electronic-structure calculations," Phys. Rev. B **41**, 5414–5416 (1990).

[47] Ian Morrison, D. M. Bylander, and Leonard Kleinman, "Nonlocal hermitian norm-conserving vanderbilt pseudopotential," Phys. Rev. B **47**, 6728–6731 (1993).

[48] A Marek, V Blum, R Johanni, V Havu, B Lang, T Auckenthaler, A Heinecke, H-J Bungartz, and H Lederer, "The ELPA library: scalable parallel eigenvalue solutions for electronic structure theory and computational sci-

ence," Journal of Physics: Condensed Matter **26**, 213201 (2014).

[49] T. Auckenthaler, V. Blum, H. J. Bungartz, T. Huckle, R. Johanni, L. Krämer, B. Lang, H. Lederer, and P. R. Willems, "Parallel solution of partial symmetric eigenvalue problems from electronic structure calculations," Parallel Computing **37**, 783–794 (2011).

[50] John P. Perdew, Kieron Burke, and Matthias Ernzerhof, "Generalized gradient approximation made simple," Phys. Rev. Lett. **77**, 3865–3868 (1996).

[51] John P. Perdew, Kieron Burke, and Matthias Ernzerhof, "Generalized gradient approximation made simple [phys. rev. lett. 77, 3865 (1996)]," Phys. Rev. Lett. **78**, 1396–1396 (1997).

[52] Steve Plimpton, "Fast parallel algorithms for short-range molecular dynamics," Journal of Computational Physics **117**, 1 – 19 (1995).

[53] D R Mason, D Nguyen-Manh, and C S Becquart, "An empirical potential for simulating vacancy clusters in tungsten," Journal of Physics: Condensed Matter **29**, 505501 (2017).

[54] Daniel R. Mason, Duc Nguyen-Manh, Mihai-Cosmin Marinica, Rebecca Alexander, Andrea E. Sand, and Sergei L. Dudarev, "Relaxation volumes of microscopic and mesoscopic irradiation-induced defects in tungsten," Journal of Applied Physics **126**, 075112 (2019).

[55] J. Byggmäster, A. Hamedani, K. Nordlund, and F. Djurabekova, "Machine-learning interatomic potential for radiation damage and defects in tungsten," Phys. Rev. B **100**, 144105 (2019).

[56] M. W. Finnis and J. E. Sinclair, "A simple empirical n-body potential for transition metals," Philosophical Magazine A **50**, 45–55 (1984), https://doi.org/10.1080/01418618408244210.

[57] Yvon Le Page and Paul Saxe, "Symmetry–general least–squares extraction of elastic data for strained materials from ab initio calculations of stress," Phys. Rev. B **65**, 104104 (2002).

[58] Ju Li, "AtomEye: an efficient atomistic configuration viewer," Modelling and Simulation in Materials Science and Engineering **11**, 173–177 (2003).

[59] D. J. Bacon, R. Bullough, and J. R. Willis, "The anisotropic elastic energy of a rhombus-shaped dislocation loop," The Philosophical Magazine: A Journal of Theoretical Experimental and Applied Physics **22**, 31–45 (1970).

[60] S. L. Dudarev, R. Bullough, and P. M. Derlet, "Effect of the $\alpha - \gamma$ phase transition on the stability of dislocation loops in bcc iron," Phys. Rev. Lett. **100**, 135503 (2008).

[61] J.P. Hirth and J. Lothe, *Theory of Dislocations* (Krieger Publishing Company, 1982).

[62] P. H. Dederichs, "The theory of diffuse X-ray scattering and its application to the study of point defects and their clusters," Journal of Physics F: Metal Physics **3**, 471–496 (1973).

[63] P. M. Derlet, D. Nguyen-Manh, and S. L. Dudarev, "Multiscale modeling of crowdion and vacancy defects in body-centered-cubic transition metals," Phys. Rev. B **76**, 054107 (2007).

[64] Jan Fikar, Robin Schublin, Daniel R. Mason, and Duc Nguyen-Manh, "Nano-sized prismatic vacancy dislocation loops and vacancy clusters in tungsten," Nuclear Materials and Energy **16**, 60 – 65 (2018).

[65] G. J. Ackland and R. Thetford, "An improved n-body

semi-empirical model for body-centred cubic transition metals," Philosophical Magazine A **56**, 15–30 (1987), https://doi.org/10.1080/01418618708204464.

[66] M-C Marinica, Lisa Ventelon, M R Gilbert, L Proville, S L Dudarev, J Marian, G Bencteux, and F Willaime, "Interatomic potentials for modelling radiation defects and dislocations in tungsten," Journal of Physics: Condensed Matter **25**, 395502 (2013).

[67] A. Stukowski, V.V. Bulatov, and A. Arsenlis, "Automated identification and indexing of dislocations in crys-

tal interfaces," Model. Simul. Mater. Sci. Eng. **20**, 085007 (2012).

[68] T. Frolov and Y. Mishin, "Temperature dependence of the surface free energy and surface stress: An atomistic calculation for cu(110)," Phys. Rev. B **79**, 045430 (2009).

[69] C.B. Barber, D.P. Dobkin, and H.T. Huhdanpaa, "The quickhull algorithm for convex hulls," ACM Trans. on Mathematical Software **22**, 469–483 (1996).

[70] M. Berger, "Geometry i," (Springer-Verlag, 1994) p. 263.